

1 **Long-term flood-hazard modeling for coastal areas using InSAR**
2 **measurements and a hydrodynamic model: the case study of Lingang**
3 **New City, Shanghai**

4
5 Jie Yin^{1,2,3}, Qing Zhao^{1,2,*}, Dapeng Yu⁴, Ning Lin⁵, Julia Kubanek⁶, Guanyu Ma², Min Liu^{1,2,3}, Antonio Pepe⁷

6
7 1 Key Laboratory of Geographic Information Science (Ministry of Education), East China Normal University, China

8 2 School of Geographic Sciences, East China Normal University, China

9 3 Institute of Eco-Chongming, East China Normal University, China

10 4 Centre for Hydrological and Ecosystem Science, Department of Geography, Loughborough University, UK

11 5 Department of Civil and Environmental Engineering, Princeton University, USA

12 6 Department of Earth and Planetary Sciences, McGill University, Canada

13 7 Institute for Electromagnetic Sensing of the Environment (IREA), National Research Council (CNR) of Italy, Italy

14

15 **Abstract:** In this paper, we study long-term coastal flood risk of Lingang New City, Shanghai, considering 100- and 1000-year coastal

16 flood return periods, local sea-level rise projections, and long-term ground subsidence projections. TanDEM-X satellite data acquired

17 in 2012 were used to generate a high-resolution topography map, and multi-sensor InSAR displacement time-series were used to obtain

18 ground deformation rates between 2007-2017. Both data sets were then used to project ground deformation rates for the 2030s and 2050s.

19 A 2-D flood inundation model (FloodMap-Inertial) was employed to predict coastal flood inundation for both scenarios. The results

20 suggest that the sea-level rise, along with land subsidence, could result in minor but non-linear impacts on coastal inundation over time.

21 The flood risk will primarily be determined by future exposure and vulnerability of population and property in the floodplain. Although

22 the flood risk estimates show some uncertainties, particularly for long-term predictions, the methodology presented here could be applied

23 to other coastal areas where sea level rise and land subsidence are evolving in the context of climate change and urbanization.

24 **Keywords:** Coastal flooding; Sea level rise; Land subsidence; InSAR; FloodMap

25

26 **1. Introduction**

27

28 The global mean sea-level has risen at an average rate of 1.6–1.9 mm/year during the 20th century (Hay et al. 2015), and
29 the rate is projected to accelerate, with a total sea-level rise (SLR) of up to 2 m over the 21st century (Oppenheimer and
30 Alley, 2016). However, the projections remain quite uncertain due to difficulties in estimating the rate of melting of glaciers
31 and the melting of the Greenland and Antarctic ice sheets. The fifth Assessment Report (AR5) of the Intergovernmental
32 Panel on Climate Change (IPCC) suggests higher SLR rates throughout this century based on recent ice-sheet observations
33 (IPCC 2014), hence increased flooding risks for low-lying coastal zones. Coastal inundation risks under sea-level rise have
34 been assessed and mapped extensively for many coastal regions, including, e.g., in Charlestown, RI, USA (Grilli et al.
35 2017), in the Italian coastal plains (Antonioli et al. 2017), in the coastal zones of Poland (Paprotny et al. 2017), in southeast
36 Queensland, USA (Mills et al. 2016), in New York, USA (Orton et al. 2015, Lin and Shullman 2017), and in Shanghai in
37 China (Wang et al. 2012).

38

39 Moreover, non-climate-related anthropogenic processes, such as ground subsidence due to groundwater extraction,
40 extensive coastal settlements in lands reclaimed from the sea, and complex subsidence phenomena related to artificial sea
41 walls, will exacerbate the flooding risk of coastal zones. There is a global consensus that land subsidence is a major problem
42 in low-lying coastal zones around the world (Jelgersma 1996; Ericson et al. 2006; Syvitski et al. 2009; Teatini et al. 2011).
43 Local sinking of land resulting from anthropogenic and natural processes, in combination with sea level rise caused by
44 climate change, makes the situation worse for coastal settlements. A large number of studies has already stressed the

45 significance of relative SLR in increasing coastal flood frequency and intensity (Karegar et al. 2017; Little et al. 2015; Shi
46 et al. 2012; Cayan et al. 2008; Carminati et al. 2002). For example, with a relative SLR from 0.5 m to 1 m predicted by the
47 2080s, a 100-year flood is projected to occur 2 to 4 times more often for New York City (Horton et al. 2015).

48
49 Recent advances in InSAR techniques (Higgins, 2016; Mason et al., 2016; Massonnet and Feigl, 1998) and the advent of
50 simplified hydraulic models have enabled high resolution scenario-based flood modeling in the context of SLR and land
51 subsidence. Remotely sensed digital elevation models (DEMs) with varying resolutions have been widely applied for flood
52 modeling (Hinkel et al. 2014; Sampson et al. 2015; Domeneghetti, 2016). Although LiDAR DEMs have optimal resolution
53 and accuracy, they do not have global coverage and are not available over broad areas, particularly in developing countries.
54 Open source DEMs with global coverage, such as Shuttle Radar Topography Mission (SRTM) and Advanced Spaceborne
55 Thermal Emission and Reflection Radiometer Global Digital Elevation Model (ASTER GDEM), have demonstrated
56 remarkable usability for large-scale flood modeling (e.g. Syvitski et al. 2009; Sampson et al. 2015). However, the 90-m
57 SRTM and 30-m ASTER DEMs have significant limitations due to their coarse vertical accuracy (around 12-18 m) (Meyer
58 et al. 2011; Tachikawa et al. 2011; Yang et al. 2011). In recent years, data from the bistatic TanDEM-X satellite mission
59 have enabled the generation of DEMs with a horizontal resolution of 12 m and a vertical accuracy of 2-4 m with global
60 coverage (Krieger et al. 2007). Moreover, time-series Differential Synthetic Aperture Radar Interferometry (DInSAR) have
61 been developed to measure Earth's surface ground displacement over large areas with high spatial resolution, on the order
62 of meters, and with a temporal repetition time of 35 days (ERS and ENVISAT/ASAR sensors) and 6 days (Sentinel-1
63 sensors) (Berardino et al. 2002; Crosetto et al. 2016). Currently, with a growing number of SAR images collected by
64 different satellite missions with peculiar looking angles and operating wavelengths, a long-term (over ten years)
65 displacement time-series can be retrieved using DInSAR techniques (Samsonov 2012; Pepe et al. 2016 a, b). In addition,
66 simplified hydrodynamic models (e.g. LISFLOOD-FP, JFLOW, FloodMap) have been increasingly used for flood

67 modeling at different scales as they can capture the dominant physics of overland flood processes and take input topography
68 in the format of a regular grid. They have been proven to perform as well as full 2-D models for the treatment of coastal
69 flooding (utilizing an unstructured mesh to represent topography), but at a substantially reduced computational cost (Bates
70 et al. 2005; Yin et al. 2016).

71

72 In this study, we used the Small Baseline Subset (SBAS) DInSAR technique to jointly analyze SAR data from different
73 sensors together with a simplified hydrodynamic model (FloodMap, Yu and Lane 2006a, b; Yu and Coulthard, 2015) to
74 investigate the evolving flood risk in a changing climate of Lingang New City in Shanghai, a recently-reclaimed coastal
75 environment. The scenarios used in this paper can be defined as series of events including different flood return periods,
76 sea level and subsidence projections, and future land use in Lingang New City. The main goals of this study are to (i)
77 provide a full characterization of surface changes over time in the coastal delta environment, (ii) derive coastal submerged
78 areas under combined SLR and land subsidence scenarios, and (iii) assess potential coastal flood impacts on a fast growing
79 waterfront urban area. The remainder of this paper is organized as follows. Section 2 describes the study area, whereas
80 Section 3 introduces materials and methods, including the DEM generation, land subsidence measurement, SLR projections,
81 and coastal flood modeling. Section 4 presents the results and discussions. Conclusions and future research directions are
82 provided in Section 5.

83

84 **2. Study area**

85

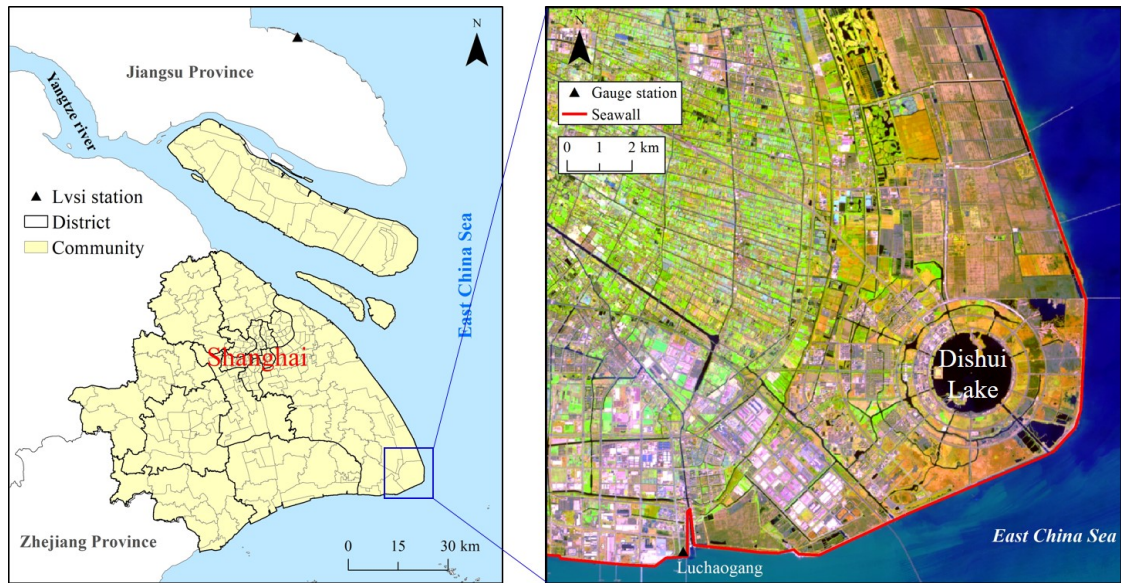
86 Lingang New City, a township at the east end of Shanghai, has been chosen as the study area, because it is highly vulnerable
87 to coastal flooding and is affected by a significant land subsidence over the past decade (Wang et al. 2012). The study site
88 is surrounded by the Yangtze River estuary, East China Sea and Hangzhou Bay (Fig. 1). It covers about 315 km² of the

89 southeast part of Pudong New Area with a flat and low-lying topography (on average about 4 m above the Wusong Datum).
90 According to China Sea Level Bulletin (2008, 2017), mean sea level in the area has been rising with an average rate of 3.8
91 mm/a during the past 30 years, and has been empirically estimated as up to 150 mm in the next 30 years. Lingang has been
92 historically experiencing variations in landscape due to changes in natural forcing and intensive human activities, such as
93 sediment deposition, erosion, sand excavation, dam construction and land reclamation (Yang et al. 2011). Human activities
94 have also greatly modified the coastal topography over the past decades. Since 2002, this area has been rapidly developed
95 to be a new sub-center for several functional zones (e.g., a Bonded Logistics Park). A large part of the region (133 km²),
96 representing approximately 42% of the total area, is sea-reclaimed land (Tian et al. 2016). The subsidence in reclamation
97 areas is dominated by soil compaction mechanisms, which are primarily responsible for vertical movements (Cai et al.
98 2008; Pepe et al. 2016a; Yu et al. 2017). Natural compaction of loose sediments and self-weight consolidation of dredger
99 fill, under intense urbanization, has caused significant land subsidence in this area.

100

101 In history, the area has been frequently affected by cyclonic storms, particularly during the flood season (June to
102 September). For example, during typhoon Winnie (1997), the storm surge peak coincided with an astronomical high tide
103 and resulted in the highest water level in record (5.66 m above Wusong Datum) at Luchaogang gauge station (Fig. 1), and
104 extensive flooding occurred in the coastal floodplain due to levee breach (Liu 2008). To protect against evolving coastal
105 floods, flood defense system in Lingang were constructed and reinforced several times over the past decades (Fan et al.
106 2017). In the 1970s, '85' (i.e., 8 m height and 5 m width levee crest) seawall has been built in response to an extreme
107 coastal flood event that occurred in August 1974. Since the end of the 20th century, higher standard seawall (i.e., around
108 10 m height) has been constructed to withstand a 200-year storm tide plus wave induced by 12-force winds.

109



110

111 Figure 1. Location of the study area

112

113 **3. Materials and methodology**

114

115 **3.1 DEM generation**

116

117 The TanDEM-X mission has the innovative capability to simultaneously acquire two SAR satellite images (bistatic
 118 acquisition mode) with short along-track baselines, which enables us to derive high-resolution DEMs of the study area.

119 With a pair of TanDEM-X images acquired on 04 November 2012, an up-to-date DEM of our study area, Lingang New
 120 City, has been generated using bistatic interferometry. The bistatic acquisition mode is characterized by illumination of an

121 area on the ground by one transmitter and the simultaneous acquisition of the backscattered signals with two receivers.

122 Compared to the monostatic acquisition mode, where only one image is acquired during every overflight of the satellite,
 123 temporal decorrelation and atmospheric disturbances, which severely affect the interferometric coherence, are significantly

124 reduced in the TanDEM-X bistatic mode (Gruber et al. 2012). Moreover, since the SAR data pair is simultaneously imaged,

125 the phase contribution due to ground deformation can be neglected. The interferometric phase is simplified in the bistatic

126 interferometry case as follows (Kubanek et al. 2015):

$$127 \quad \phi = \phi_{ref} + \phi_{topo} + \phi_{noise} \quad [1]$$

128 where ϕ_{ref} is the phase of the reference surface, i.e., WGS 84 (World Geodetic System 1984) ellipsoid; ϕ_{topo} is the
129 topographic phase; and ϕ_{noise} is the phase noise.

130 We generated the interferogram with the TanDEM-X pairs using the DORIS software packages (Kampes et al. 2003). The
131 interferometric phase can be expressed as follows (Kubanek et al. 2015):

$$132 \quad \phi = -\frac{2\pi}{\lambda} \Delta r \quad [2]$$

133 where Δr is the path length difference between the two (bistatic) SAR acquisitions and λ is the wavelength, which is 3.1
134 cm for TanDEM-X. Before phase unwrapping, i.e., before resolving the ambiguous phase, a Goldstein filter (Goldstein and
135 Werner, 1998) was applied to smooth the interferometric phase. The filtered interferogram was unwrapped using the
136 SNAPHU (Statistical-Cost Network-Flow Algorithm for Phase Unwrapping) algorithm (Chen and Zebker, 2001).
137 Subsequently, the path length difference of Eq. 2 was converted from phase-to-height (Bamler and Hartl 1998;
138 Franceschetti and Lanari 1999):

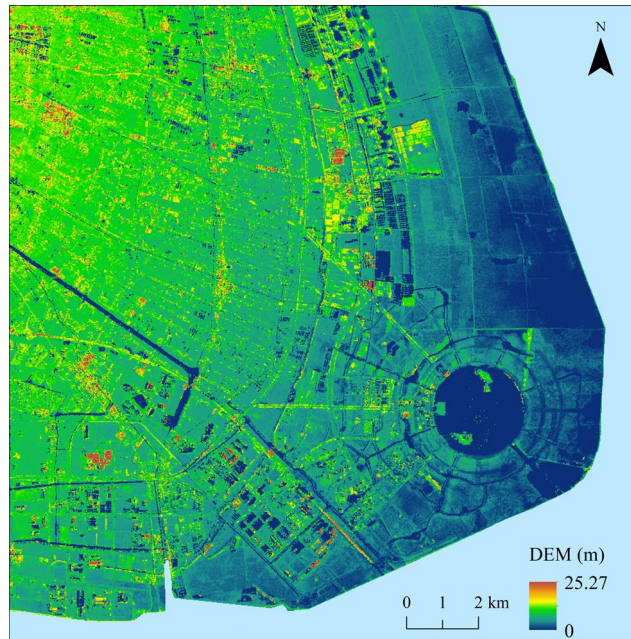
$$139 \quad h = -\frac{\lambda}{2\pi} \frac{R \sin \vartheta}{b_{\perp}} \psi \quad [3]$$

140 where b_{\perp} is the orthogonal baseline of the InSAR pair, R is the sensor-to-target slant-range distance, ϑ is the sensor side-
141 looking angle, ψ represents the unwrapped phase relevant to the interferometric phase ϕ (compensated by the phase of
142 the reference plane), and h is the surface height.

143

144 The obtained topographic map h is then geocoded to geographic coordinates (WGS 84) using DORIS and gridded using
145 GMT (Wessel et al. 2013). A grid spacing of 6 m is selected for the DEM product and it is further resampled to 18 m
146 resolution to reduce computational costs. Fig 2 shows the generated Tandem-X DEM of the study area. The theoretical
147 accuracy and actual DEM performance of bistatic TanDEM-X InSAR were verified by Weigt et.al. (2012). Their

148 verification shows that for slopes less than 20%, the height error is predicted to be 1.7 m and 2.5 m for a height of ambiguity
149 of 30 m and 45 m, respectively, for the global TanDEM-X data set. Kubanek et al. (2017) obtained a standard deviation of
150 1.63 m for elevation differences of TanDEM-X DEMs that were generated to study the Tolbachik volcanic complex in
151 Kamchatka, Russia, using the same methodology as used for DEM generation presented in this paper.



152

153 Figure 2. The generated Tandem-X DEM of the study area

154

155 3.2 Long-term ground settlement measurement

156 Advanced time-series DInSAR algorithms can rapidly and regularly detect and measure ground deformation with a high
157 accuracy and at different scales (Ferretti et al. 2001; Berardino et al. 2004; Hooper et al. 2012). DInSAR techniques have,
158 among others, been applied for measuring and mapping ground deformation caused by over-pumping underground water
159 (Gourmelen et al. 2007), tectonic movement (Fattahi et al. 2015), sediments consolidation of river deltas (Aly et al. 2012),
160 and land reclamation (Zhao et al. 2015). Time-series DInSAR techniques have been proven being effective approaches for
161 accurately measuring ground deformation (Casu et al. 2006; Zhao et al. 2014).

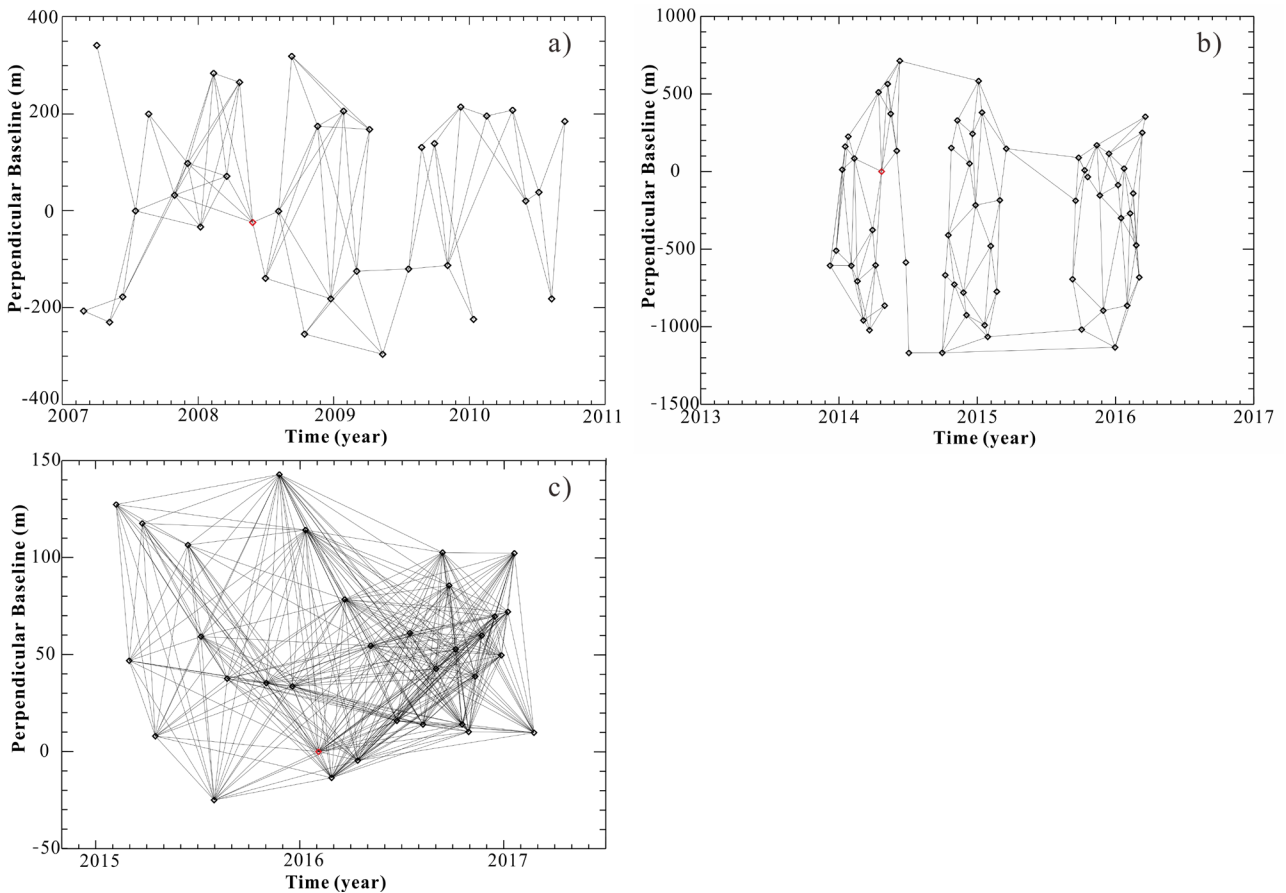
162

163 3.2.1 Multi-platform SAR displacement time-series

164

165 Three independent sets of SAR images, acquired by different satellites, were used to retrieve long-term ground
166 displacement of Lingang New City. The former consists of 35 ENVISAT ASAR (ENV) images, acquired with ascending
167 passes from February 26, 2007 to September 13, 2010. The second SAR set is composed of 61 COSMO-SkyMed (CSK)
168 images, which were collected with descending passes from December 7, 2013 to March 18, 2016. The third set was
169 collected by the Sentinel-1A (S1A) satellite with ascending passes from February 26, 2015 to April 4, 2017. All available
170 SAR images were processed through the well-known Small BAseline Subset (SBAS) multi-temporal DInSAR technique,
171 which is outlined in the next subsection.

172



173

174 Figure 3 Distribution of the available ENVISAT ASAR, COSMO-SkyMed, and Sentinel-1A SAR data in the temporal-

175 perpendicular baseline plane, as depicted in a), b), and c) respectively. The master images of ENVISAT ASAR, COSMO-
176 SkyMed, and Sentinel-1A SAR data are represented by red diamonds.

177

178 3.2.2 Small BAseLine technique

179

180 Small Baseline (SB) techniques are a class of advanced time-series DInSAR methods (Mora et al. 2003; Usai 2003;
181 Berardino et al. 2002). In particular, the SBAS algorithm (Berardino et al. 2002, Lanari et al. 2007) is one of the well-
182 known and highly used SB techniques. This algorithm is based on selecting a set of small temporal and perpendicular
183 baseline interferograms, thus mitigating decorrelation phenomena, and allows the generation of mean deformation velocity
184 maps and relevant displacement time-series for each coherent point. Fig. 3 (a)-(c) show the distribution of the three groups
185 of SAR images used in this study in the temporal/perpendicular baseline plane. The small baseline interferometric SAR
186 data pairs might be arranged in a few subsets. In order to generate a unique displacement time-series, the phase ambiguities
187 of the differential SAR interferograms are preliminarily resolved, i.e., unwrapped (Costantini and Rosen, 1999, Pepe and
188 Lanari 2006) and subsequently combined using the singular value decomposition (SVD) method. The residual topographic
189 and atmospheric phase artifacts are also estimated and filtered out. The DInSAR products, i.e., the mean deformation
190 velocity maps and the relevant displacement time-series, are finally geocoded to a common spatial grid. Interested readers
191 can find a detailed description of the SBAS approach and the processing chain in Berardino et al. (2002).

192

193 3.2.3 Multi-platform time-series DInSAR

194

195 After the SBAS processing of the independent SAR datasets, the unique deformation time-series spanning the acquisition
196 times of the overall SAR datasets is, however, still unknown. Indeed, it should be noted that the deformation time-series

197 are relative to the first SAR acquisition time of each independent dataset. In order to combine the deformation time-series
 198 obtained by multi-platforms, we need to determine the multi-platform deformation time-series relative to one global
 199 reference time. A methodology has been developed by Pepe et al. (2016a) to combine two time-gapped deformation time-
 200 series obtained by ENVISAT ASAR and COSMO-SkyMed SAR datasets. To this aim, the DInSAR-derived line-of-sight
 201 (LOS) deformation time-series was first independently projected into vertical deformation time-series by assuming the
 202 horizontal (east-west) deformation is negligible. Then, an external geotechnical centrifuge model (Yang 2008), representing
 203 a complete time-settlement curve in reclaimed areas of Shanghai, was exploited and fitted to data to jointly estimate the
 204 unique deformation time-series over the entire time period between 26 February 2007 and 18 March 2016 (Zhao et al. 2015,
 205 Pepe et al. 2016a). Note that deformation due to reclamation can be distinguished in the primary consolidation phase, which
 206 takes place immediately after the completion of the reclamation process, and in the secondary compression stage of the
 207 alluvial deposit creep of the reclamation fill (Yang 2008), which can last several years after the completion of the
 208 reclamation procedures. The used laboratory centrifuge model permits to analyze the temporal evolution of the (vertical)
 209 ground displacement due to the self-weight consolidation (including both the primary and secondary compression stages)
 210 of the ocean-reclaimed lands. The used model is expressed as follows (Zhao et al. 2015):

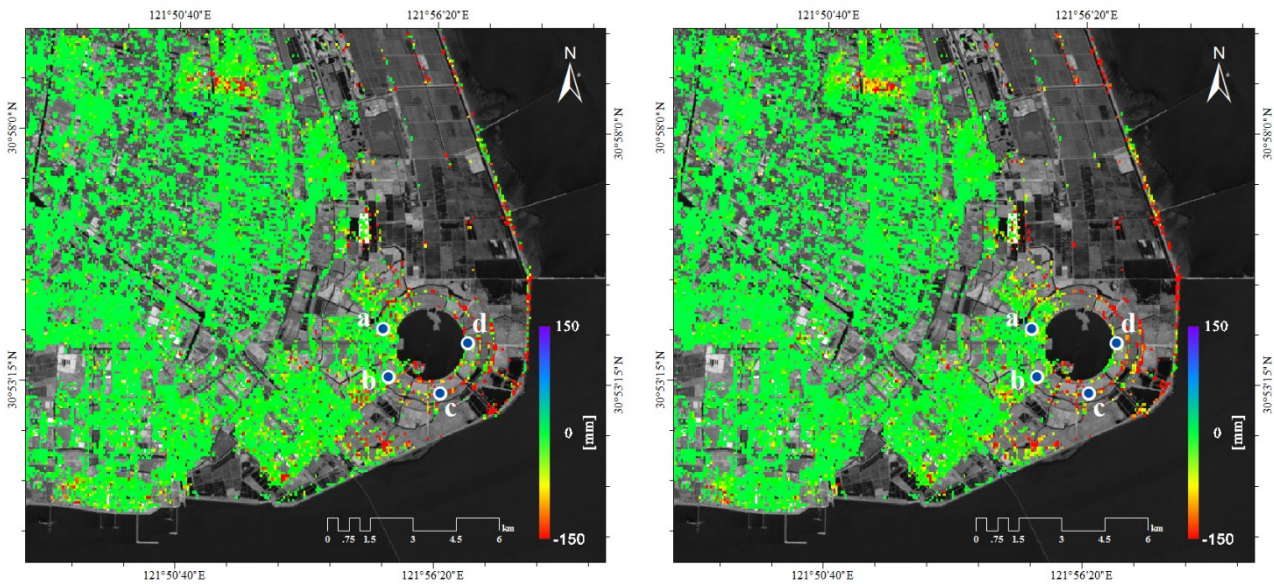
$$211 \quad s(t) = S_m \frac{(t - \delta)^\mu}{k^\mu + (t - \delta)^\mu} \quad [4]$$

212 where t represents the consolidation time, S_m is the asymptotic (cumulative) deformation assumed at infinite time (i.e.,
 213 when the soil consolidation process is ended), δ accounts for the (variable) starting time of the reclamation process, and
 214 k and μ are model parameters that influence the shape and curvature of the time-dependent model.

215
 216 First, the combined ENV+CSK deformation time-series were determined, for each radar pixel, by finding the best-fit
 217 between the geotechnical model and the multi-platform deformation time-series. The nonlinear optimization problem was
 218 solved efficiently through the (iterative) Levenberg–Marquadt least squares (LS) minimization technique. Subsequently,

219 the Sentinel-1A displacement time-series was independently generated by applying the SBAS technique, converted into
 220 (vertical) displacement time-series and finally combined to the previously obtained ENV+CSK displacement time-series.
 221 This procedure is repeated for each coherent radar pixel of the investigated scene. Due to the time overlap between the
 222 combined ENV+CSK and S1A subsets, the time-series were linked using SVD by extending what was originally proposed
 223 in Berardino et al. (2002). Finally, the long-term deformation time-series with a time-span of approximately 10 years (from
 224 2007 to 2018) were obtained. Fig. 4 (a)-(b) show the maps of the asymptotical ground deformation, namely the term of the
 225 best-fit model between the combined ENV+CSK and ENV+CSK+S1A displacement time-series and the model,
 226 respectively. As evident, there is a good agreement between the two maps, thus indicating that the Levenberg-Marquadt
 227 LS optimization procedure is robust to data. Additional remarks and the discussion of the DInSAR results are presented in
 228 Section 4.3.

229



230

231 Figure 4. Maps of asymptotic ground deformation from Nov 2012 to the end time of the consolidation phase derived with
 232 the best fit model constrained by ENV+CSK (left) and ENV+CSK+S1A (right)

233

234 Additionally, some measurements of the displacement affecting the seawalls, as gathered from leveling measurement

235 campaigns in 2009 (Chen et al. 2016), were also available to us. Figure 5 (a)-(b) shows the vertical mean deformation rate
 236 of the seawalls as seen from the leveling and the SBAS measurements (Zhao et al. 2015). It should be noted that we show
 237 the distribution of high-coherent pixels seen by ENVISAT in Figure 5(b) because the available corresponding leveling
 238 measurements span approximately the same time period of the ENVISAT acquisitions. The cross comparison between
 239 leveling and SBAS data shows a good agreement. Finally, starting from the retrieved parameters and the time vector t of
 240 the best-fit model of Equation (3) (see Zhao et al., 2015 for additional information), the expected cumulative deformations
 241 (calculated with respect to 26 February 2007) for January 1st of 2030 and 2050, respectively, were predicted.

242

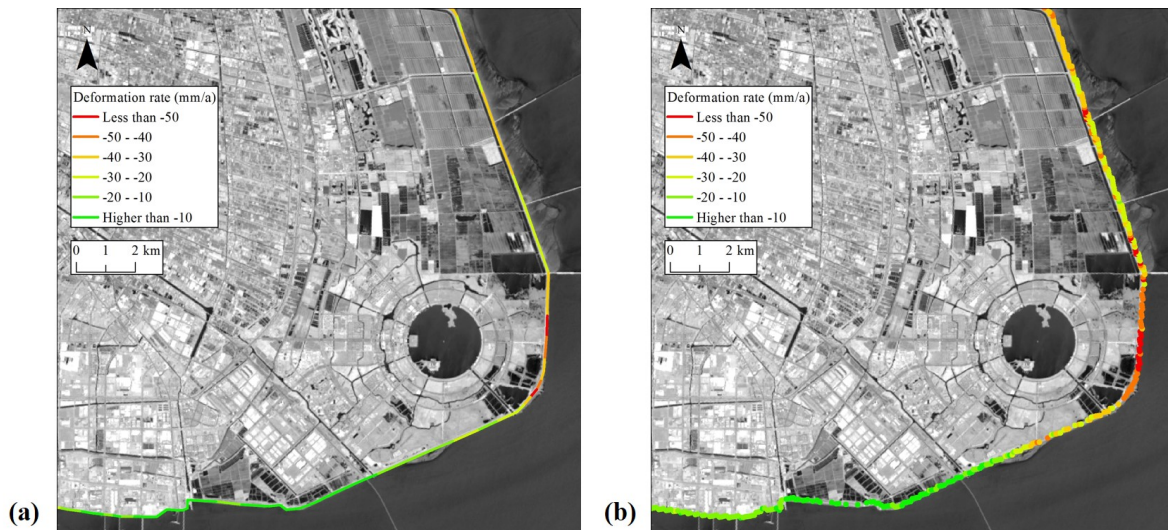


Figure 5 Vertical deformation rate of the seawall obtained by leveling measurements (a) and SBAS-ENVISAT (b)

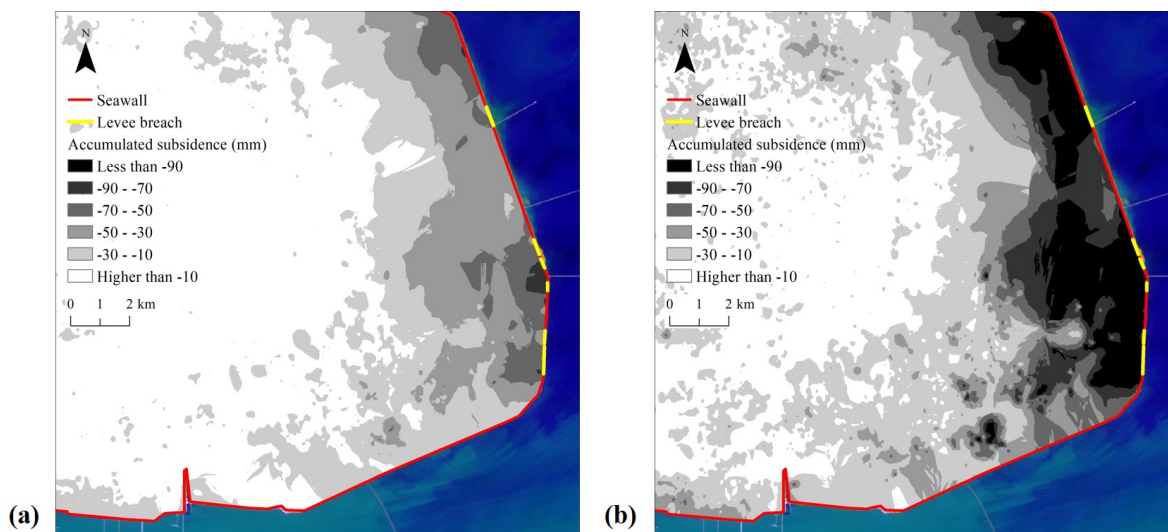


Figure 6 Accumulated ground deformation projections for 2030s (a) and 2050s (b) in Lingang New City

243

244 **3.3 Sea level rise projections**

245

246 Sea level change shows significant local or regional differences due to both climate change and non-climatic factors such
247 as land processes, ocean circulation and atmospheric pressure (Cooper et al. 2008; Hallegatte et al. 2011). Recently, Kopp
248 et al. (2014) presented a global set of probabilistic local sea-level projections which quantified SLR contributions from
249 global processes (e.g., the thermal expansion of ocean water) to local factors (e.g., glacial isostatic adjustment). It has been
250 widely used for flood risk analysis (e.g., Lin and Shullman 2017). The dataset includes 17 station-based SLR projections
251 in China's coastal areas, among which one station (Lvsi) located at the Yangtze River Estuary. We use the SLR projection
252 of this station in the present study. Compared to the aforementioned statistical SLR studies (e.g. Li et al. 1998), Kopp et al.
253 (2014) show a significant higher rise in local sea level. To account for plausible extreme conditions, we adopted the high-
254 end estimates (i.e., 95th percentiles of model-based distributions) of Kopp's SLR projection at Lvsi for the 2030s (0.31 m)
255 and 2050s (0.61 m), the two future time frames considered in this study.

256

257 **3.4 Coastal flood modeling**

258

259 In order to derive coastal flood inundation, FloodMap-Inertial, a well-established 2D hydrodynamic model was employed
260 in this study (Yu and Lane 2011). This model, as well as an earlier diffusion-based version of it (Yu and Lane 2006a, b),
261 has been extensively applied in a number of different environments such as coastal regions, urban areas and basins (e.g.,
262 Casas et al. 2010; Yin et al. 2013, 2016a, 2016b). It is raster-based and solves the inertial form of the 2D shallow water
263 equations. Flood routing takes the same form as the inertial algorithm of Bates et al. (2010), but with a slightly different

264 method to calculate the time steps. The details of the model are described in Yu and Lane (2011). Therefore, we only focus
 265 on the major features of the model. Neglecting the convective acceleration term in the Saint-Venant equation, the
 266 momentum equation becomes:

$$267 \quad \frac{\partial q}{\partial t} + \frac{gh\partial(h+z)}{\partial x} + \frac{gn^2q^2}{R^{4/3}h} = 0 \quad [5]$$

268 where q is the flow per unit width, g is the acceleration due to gravity, R is the hydraulic radius, z is the bed elevation,
 269 h is the water depth, and n is the Manning's roughness coefficient. R can be approximated with h for wide and shallow
 270 flows. Discretizing the equation with respect to time produces:

$$271 \quad \frac{q_{t+\Delta t} - q_t}{\Delta t} + \frac{gh_t\partial(h+z)}{\partial x} + \frac{gn^2q_t^2}{h_t^{7/3}} = 0 \quad [6]$$

272 where one of the q_t in the friction term can be replaced by $q_{t+\Delta t}$, resulting in the explicit expression of the flow at the
 273 next time step:

$$274 \quad q_{t+\Delta t} = \frac{q_t - gh_t\Delta t\left(\frac{\Delta(h+z)}{\Delta x}\right)}{(1 + gh_t\Delta t n^2 q_t / h_t^{10/3})} \quad [7]$$

275 The flow in the x and y directions are decoupled and take the same form. Discharge is evaluated at cell edges and depth at
 276 the cell center.

277
 278 To apply FloodMap for coastal flood simulation, time-series of water level along the land-sea boundary are used as input
 279 to drive 2D inland flow routing. The shape of the stage hydrograph at the boundary section was derived from the hourly
 280 recorded water level available at Luchaogang gauge station during Typhoon Winnie. Assuming tidal cycles remain constant,
 281 time-series of the 100- and 1000-year design flood heights above Wusong Datum were generated by scaling Typhoon
 282 Winnie's surge heights. To balance the accuracy and computational costs, 24-hour stage hydrographs, including two rising
 283 phases and two falling limbs, were applied to simulate the coastal flood processes. To account for the effect of SLR, the
 284 projected SLRs were linearly added to the state of 2012 to create the flood scenarios for the 2030s and 2050s. Due to lack

285 of available verification materials (e.g., high watermarks and observed flood extent) in the study area, an empirically-based,
286 relatively low floodplain roughness value of 0.03 which corresponds to the Manning roughness coefficient, was used in
287 the simulations to represent the effect of tidal-flat area and open land on coastal flood routing.

288

289 Given the high design standard of seawalls built along the coastline of Shanghai, coastal flooding was not expected to
290 affect the region significantly, assuming seawalls are intact during storm surge events. Comparison of seawall heights (both
291 with and without land deformation) and projected peak surge values suggest that future storm surge events of up to 1000-
292 year magnitude would only affect the region marginally. However, coastal flooding did occur historically (e.g., 1997
293 Typhoon Winnie) along this part of the coastline, due to seawall breaching. Therefore, we generated breaching scenarios
294 based on the actual conditions of the seawalls obtained from a field survey and the observed & projected deformation rates
295 (Fig. 5 and 6). According to 'Code for design of sea dike project (GB/T 51015-2014)' in China, sections with subsidence
296 rates higher than 50 mm/a, which were in particular vulnerable to burst under the combined effect of wave and storm surge,
297 were removed from the seawall system in the simulation.

298

299 **3.5 Flood sensitivity analysis**

300

301 Due to the scenario-based nature of this study, we used a theoretically most appropriate roughness value (i.e., 0.03) in flood
302 modeling. However, in the context of flood inundation modeling for historical events, floodplain friction was found to
303 introduce bias into the modeling results. Therefore, model sensitivity to roughness parameterization was evaluated with
304 FloodMap by varying the Manning's n values (between 0.01 and 0.1 at a 0.01 interval).

305

306 In order to detect the spatio-temporal changes in flood inundation, two metrics (i.e., Fit statistic (F) and Root Mean Square

307 Deviation (RMSD)) were used to quantify the degree of matching and variation between model predictions respectively.
308 In each case, the n=0.01 simulation was used as the reference and both measures are calculated against this reference. F is
309 widely used for evaluating the goodness of agreement between predicted flood extent and the reference (Bates and De Roo,
310 2000; Horritt and Bates, 2001; Yu and Lane, 2006). It varies between 1 for a perfect fit and 0 when no overlap exists. It can
311 be calculated as follows:

$$312 \quad F = \frac{A_o}{A_r + A_s - A_o}$$

313 where A_r is the referenced wet areas, A_s is the predicted wet areas, and A_o is the overlap of A_r and A_s .

314

315 The RMSD is particularly suitable for evaluating the overall agreement/discrepancy of water depth between two paired
316 results on a cell-by-cell basis (Yu and Lane, 2011; Yin et al. 2016). It can be defined as follows:

$$317 \quad \text{RMSD} = \sqrt{\frac{\sum_{i=0}^n (d_i^s - d_i^r)^2}{n}}$$

318 where d_i^s and d_i^r are the predicted and referenced water levels (or depths) respectively, i is the index of the wet cells and
319 n is the total number of wet cells in the prediction and observation.

320

321 **4. Results and discussions**

322

323 **4.1 Coastal inundation mapping**

324

325 Predicted maximum inundation depths for 100-year and 1000-year coastal flood scenarios due to hypothetical levee
326 breaches for the present (i.e., 2012), the 2030s and the 2050s are shown in Fig. 7 and the maximum flooded areas are
327 summarized in Table 1. The mean maximum flood depth in the table represents the average value of maximum flood depths
328 in all grids during the flood model run. Comparison of the derived inundation maps leads to two important findings. First,

329 similar inundation pattern are generally observed for both simulations (one in 100- and 1000-year return periods) in the
 330 study area, but with different flood depths. This can be largely attributed to the topographic confinement of the coastal
 331 floodplain. The levee-breach flow would be blocked by the previous seawall (Fan et al. 2017), and thus the water would
 332 be mostly confined within the coastal flat and low-lying areas where land was only recently reclaimed in the past decade
 333 (Zou et al. 2007). In addition, Dishui Lake which has a total area of 5.56 km² and a storage of 16.2 million m³, also shows
 334 a significant impact on the detention and storage of the storm water, restricting further inland propagation of coastal flood
 335 waves.

336

337 Table 1 The areas (km² and percentage of computation domain) and depths subject to different levee-breach coastal flood
 338 scenarios under sea level rise and land subsidence projections for Lingang New City, Shanghai

339

Time	High-end sea level rise (m)	Mean land subsidence (m)	Maximum flood areas (km ²) and percentage (%)		Mean maximum flood depths (m)	
			100y flood	1000y flood	100y flood	1000y flood
2012	/	/	32.79 (13.14%)	34.30 (13.74%)	1.33	1.45
2030	0.31	0.13	34.72 (13.91%)	36.37 (14.57%)	1.44	1.59
2050	0.61	0.28	37.76 (15.13%)	42.18 (16.90%)	1.56	1.76

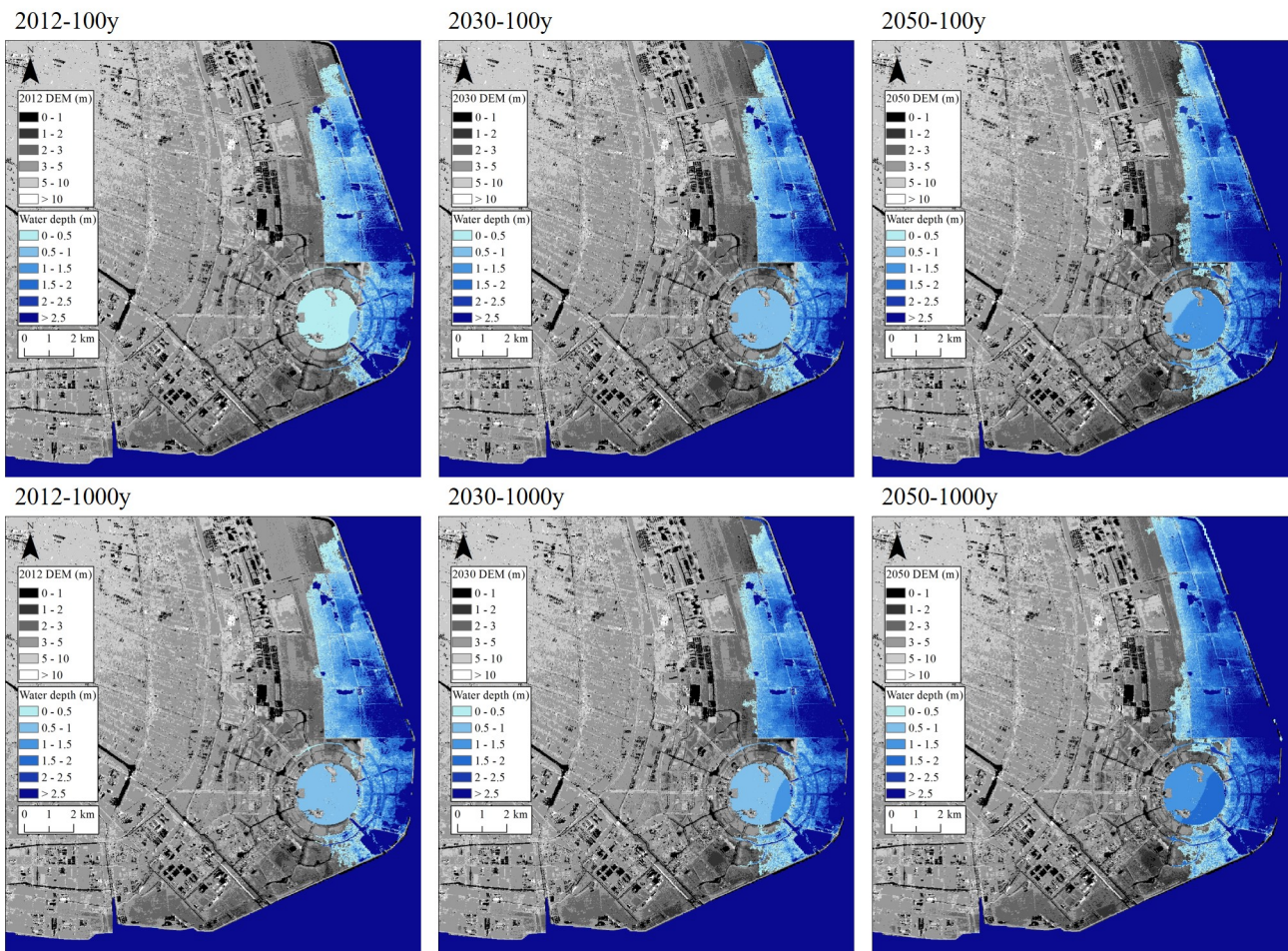
340

341 Second, our results show that rapid sea-level rise combined with extensive land subsidence generally leads to minor but
 342 non-linear impacts on coastal inundation over time in our study area. For example, when the 0.44 m and 0.89 m rise in the
 343 relative sea level (i.e. the sum of SLR and subsidence projections) for the 2030s and the 2050s are considered, a 6% and
 344 15% increase in predicted maximum inundation area can be observed for future 100-year flood events. Similarly, compared
 345 to 2012, the mean water depths are projected to rise 0.11 m (8%) by 2030 and 0.23 m (17%) by 2050, respectively. In
 346 contrast, the impact of the projected relative sea level rise appears to be more pronounced for 1000-year flood events,
 347 where the total flood area is expected to increase by 23% by 2050; the maximum water depth will rise by 21%. Although
 348 mean land subsidence only makes up around 30% of the relative sea level rise, coastal flooding response is also controlled

349 by a non-uniform pattern of subsidence. It was found that rapid subsidence would further accentuate inundation extent and
350 depth in the reclamation area, making it more vulnerable to coastal flooding.

351

352 In order to detect the temporal changes of coastal flood dynamics, the time evolution of predicted inundation areas for all
353 scenarios are presented in Fig. 8. The curves mostly coincide during the initial wetting phase (up to 7 h), suggesting that
354 levee-breach water flow extends progressively overland before and after the first flood peak, due to the mild relief and flat
355 topography of the coastal floodplain. After the rapid inland intrusion in each simulation, the inundated area increases only
356 slightly with a much higher stage during the second rising phase, indicating that further widespread expansion of coastal
357 flooding is limited due to strong resistance from surface obstruction. This finding also confirms the topographic
358 confinement of the coastal floodplain, which we identified in Fig. 2. Moreover, as shown in Fig. 8, the general pattern of
359 simulated time series revealed that the temporal characteristics of the inundated area is not strictly synchronous with the
360 timing of the tidal cycle. In most cases, the flood extent continues to increase even as the stage recedes, because the
361 floodwater level greatly overwhelmed low-lying waterfront ground. Another important finding is that the relative SLR
362 provides an elevated base for a storm flood to build upon and SLR and land subsidence may lead to more pronounced
363 impact on coastal inundation during the falling limbs of tidal hydrograph (Yin et al. 2013).



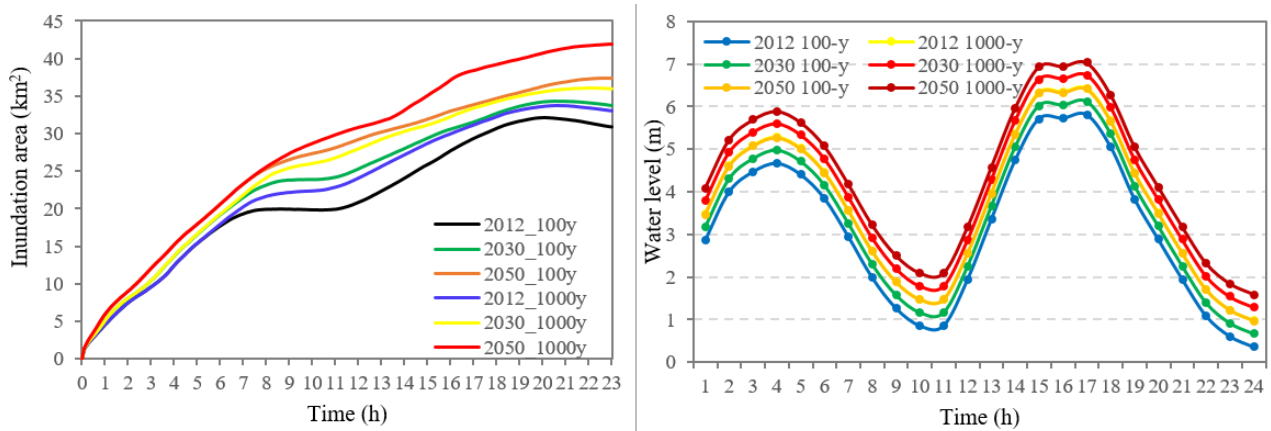
364

365 Figure 7 Potential levee-breach 100-year and 1000-year coastal flood inundation scenarios modeled with up-to-date and

366 high resolution DEM and long-term DInSAR derived ground deformation time series for Lingang New City of Shanghai

367 in 2012, the 2030s and the 2050s

368



369

370 Figure 8 Time series of inundation extents and water levels with 100-year and 1000-year flood return periods in 2012,

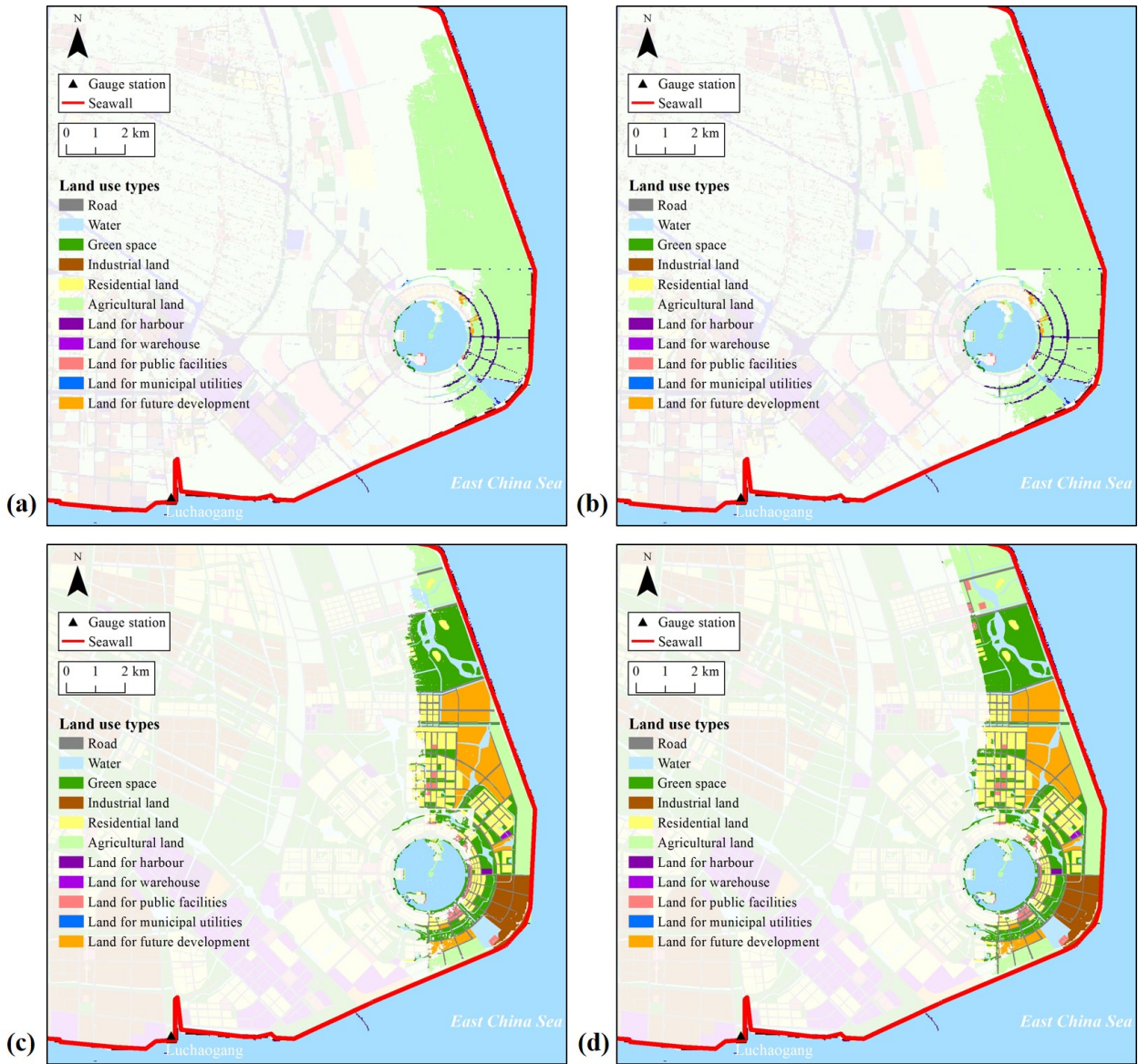
371 2030s and 2050s for Lingang New City of Shanghai

372

373 **4.2 Coastal flood impacts**

374

375 Coastal floodings, as derived by our models, will affect areas of current and future land use, where data are officially
376 provided by the Shanghai Institute of Surveying and Mapping (Fig. 9). An immediate finding is that although the Lingang
377 area has experienced rapid urbanization during the last decade, wetlands and bare lands mainly dominate the floodplain
378 and therefore flood impacts have a minor effect on the coastal communities. At present, considerable personal injury and
379 property damage are unlikely to occur in this area. However, according to the land use planning for Lingang New City, the
380 process of urbanization and floodplain development is expected to accelerate in the near future. According to the Lingang
381 New City Plan, the total population is expected to rise from about 50-100 thousand today to 1-1.5 million in the next
382 decades. Thus rapid expansion in human settlements is expected to occupy the waterfront areas around Dishui Lake. If
383 long term subsidence combined with strong storm tide causes the emergence of levee breach, extensive coastal flood
384 inundation would occur throughout the area in the 2030s and 2050s, leading to significant casualties and losses. In addition,
385 future flood risk could also be significant in the northern part of the coastal floodplain, where comprehensive industrial,
386 research & development, service, and residential areas may be constructed in the future. Compared to the direct impacts,
387 possible indirect consequences, such as interruption of public services or negative influences on industrial production and
388 living, would be more pronounced. The indirect impacts may last a few days to even a few months after an extreme event
389 (Yin et al. 2016b).



390

391 Figure 9 Land uses/planning fall within the predicted inundation areas (highlight) at current and future states: a) 100y flood

392 in 2012; b) 1000y flood in 2012; c) 100y flood in 2050s; and d) 1000y flood in 2050s

393

394 4.3 Uncertainty and limitations

395

396 Uncertainties are inherent in a changing environment. In our study, the long term flood-risk mappings could be highly

397 uncertain due to the assumptions and limitations associated with data and methods used here. First, in terms of SLR

398 projections, the response of the Greenland and the West Antarctic ice sheets to future global warming is the largest long-

399 term source of uncertainty. Although the likelihood of the ice sheet collapse within the coming century has been described
400 as extremely low (black swan, i.e., an event or occurrence that deviates beyond what is normally expected of a situation
401 and is extremely difficult to predict), a partial or complete collapse of the Western Antarctic Ice Sheet will cause the global
402 mean sea level to rise up to 4 m (Bentley, 1998; Vaughan and Spouge, 2002; Pfeffer et al. 2008; Bamber et al. 2009; Ritz
403 et al. 2015; DeConto and Pollard, 2016). Second, coastal storminess is projected to change with climate change (Lin et al.
404 2012, 2015). Future frequency of extreme storms is very likely to increase until 2100 (IPCC 2012). It is yet unclear how a
405 changing storminess, in combination with SLR, will affect the frequency and intensity of coastal flooding in Shanghai.
406 Third, the flood modeling conducted in this study is based upon an arbitrary assumption that levee breaches will occur in
407 the locations/sections with an observed subsidence rate higher than 50 mm/a. There are certain limitations and errors
408 associated with such hypothesis, as the mechanism of seawall failure is determined by different triggering factors, including
409 material and structure of the seawall, geologic conditions, and hydrodynamics (e.g., waves). The impacts of land subsidence
410 on the stability of seawall and the threshold of levee breaches should be explicitly tested and verified.

411

412 Another source of uncertainty arises from the long-term (over twenty years) ground deformation projections. Although the
413 long-term vertical deformation is predicted with best-fit models, which are obtained using the time-dependency laboratory
414 models constrained by multi-platform DInSAR measurements (Pepe et al. 2015), uncertainties in estimating the asymptotic
415 values of deformation might depend on the temporal length of the available, constrained DInSAR time-series. The longer
416 the DInSAR displacement time-series the more accurate is the fit between the DInSAR data and the foreseen models. To
417 get an idea of such uncertainties, we calculated the asymptotic ground deformation values of each high coherent point from
418 November 2012 until the end of the consolidation phases with the best-fit models constrained by the combined ENV+CSK
419 and ENV+CSK+S1A deformation time-series. As anticipated in Section 3.2.3, Fig. 4 shows the maps of asymptotic ground
420 deformation, indicating that the asymptotic values of deformation agree well with the best fit models derived by ENV+CSK

421 and ENV+CSK+S1A in most of the study areas. Most of the points with different asymptotic values (see Equation (3)) of
 422 deformation are located along the seawall and the east of Dishui Lake. In particular, Table 2 presents the asymptotic values
 423 of deformation at four points labeled as a, b, c, d in Fig. 4. According to the quantity values of uncertainties in ground
 424 deformation prediction, the observed deviation is acceptable for the long-term flood-risk mapping. It is worth remarking
 425 that our predictions are based on the analysis of only ten years of data, and are relevant to a very dynamical coastal area
 426 that is highly affected by human activities. More lands are expected to be reclaimed along the current coastline in future
 427 decades. Accordingly, continuous DInSAR measurements are necessary for monitoring and progressively measuring the
 428 changes and for updating the projections.

429

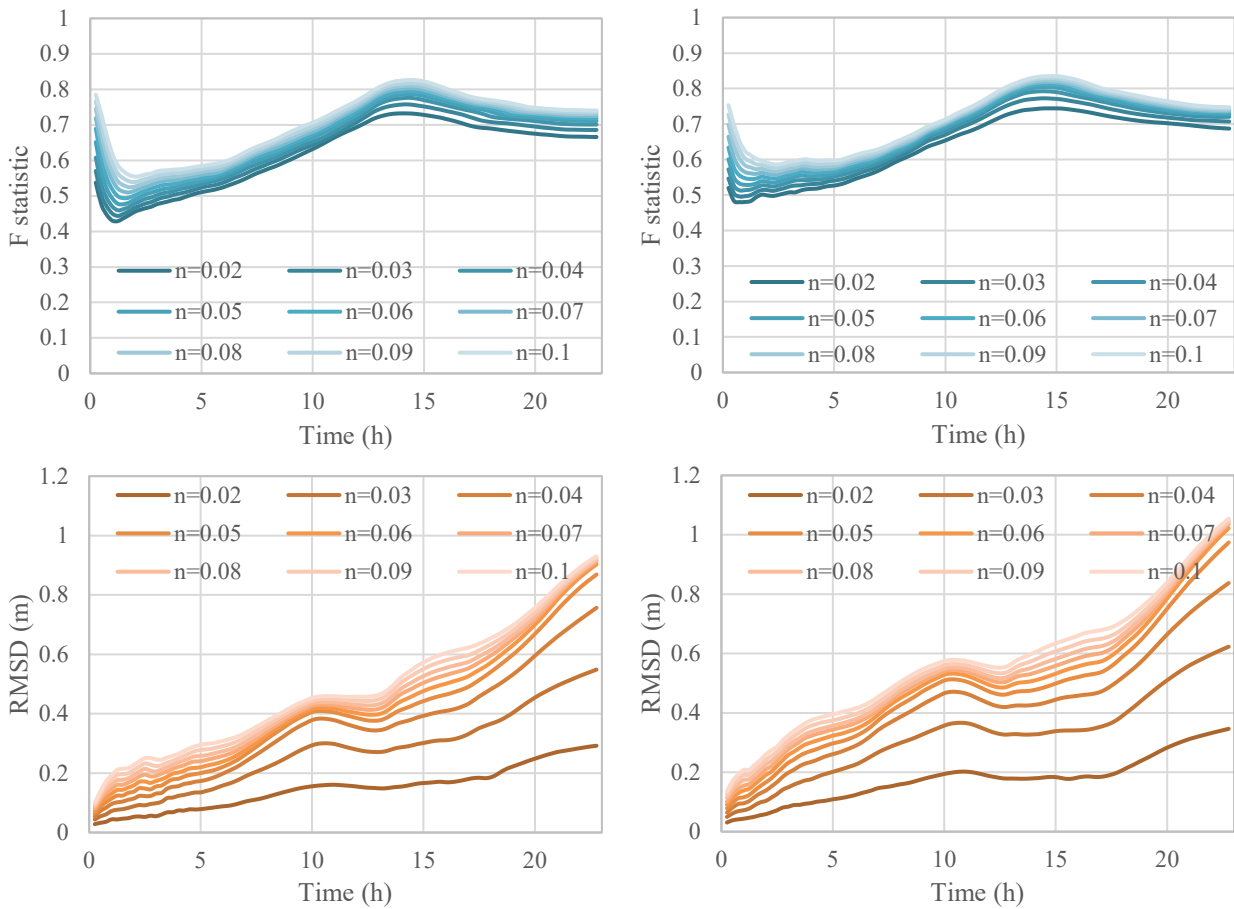
430 Table 2 Total cumulative deformation values and end time values of consolidation phases between the best-fit models
 431 retrieved by using the combined ENV-CSK time series and the ones extracted from the combined ENV-CSK-S1A time
 432 series. The end of consolidation phase has been considered, for each radar pixel, as the time in correspondence to which
 433 the expected surface displacement rate is smaller than 0.5 mm/year.

		Best fit model derived with ENV+CSK	Best fit model derived with ENV+CSK+S1A
a	End time of consolidation	2015	2015
	Asymptotic values of ground subsidence (mm)	2	2
b	End time of consolidation	2030	2031
	Asymptotic values of ground subsidence (mm)	62	60
c	End time of consolidation	2035	2035
	Asymptotic values of ground subsidence (mm)	93	109
d	End time of consolidation	2060	2057
	Asymptotic values of ground subsidence (mm)	118	109

434

435 Flood model uncertainties have been addressed and time-series of F-statistic and RMSD for each simulation are shown in
 436 Fig. 10. The results show significant variations in the spatio-temporal pattern between individual simulations and the
 437 $n=0.01$ reference, suggesting the model's strong sensitivity to floodplain roughness. Another finding is that with higher

438 Manning's n values, the differences in inundation area and depth becomes less pronounced throughout the simulations,
 439 especially in terms of RMSD. The sensitivity of the RMSD is progressively magnified as the flood magnitude increases
 440 over time. On the contrary, higher magnitude flood events (e.g., 1000-year floods) appear to be less sensitive to roughness
 441 due to the lateral confinement of the floodplain. This observation reveals that coastal flood inundation is highly uncertain
 442 in the rapidly developing area, particularly for long-term predictions.



443
 444
 445 Figure 10 Time series of F statistic, and depth RMSD for current 100- (left column) and 1000-year (right column) flood
 446 simulations with different Manning's n values

447
 448 **5. Conclusions**

449
 450 This paper demonstrates a novel approach to evaluate evolving flood hazard in the context of sea level rise and land

451 subsidence for Lingang New City in Shanghai through an integration of 2D numerical flood modeling and InSAR
452 techniques. A number of conclusions can be drawn from the results obtained in this study. First, even with rapid sea level
453 rise and extensive land subsidence in the future, coastal flood inundation due to potential levee breach is predicted to occur
454 mostly in the waterfront low-lying areas, because of topographic confinement in the floodplain and blockage of previous
455 seawalls. Second, flood impacts in this area are expected to be minor due to a very low exposure of the population and
456 property at present, but future flood risk could be significantly higher as rapid urbanization and large-scale coastal
457 development have been planned in the floodplain. Finally, limitations, biases and even errors in local SLR projections,
458 storm climatology projections, levee breach estimations, ground deformation predictions, and coastal flood modeling may
459 have induced substantial uncertainties in the final estimates.

460

461 The methodology proposed here could be applied to other coastal communities facing significant SLR, subsidence and
462 flooding challenges. It may contribute to a better understanding of the long-term coastal flood hazard at local scale, and
463 thus help to develop sustainable flood risk management in coastal communities. However, to derive more robust
464 conclusions, further research should include: (1) analyzing the mechanisms and probabilities of seawall failure to provide
465 a more complete picture of levee breach; (2) evaluating the impacts of extreme SLR scenarios (e.g., collapse of the West
466 Antarctic Ice Sheet) and projected storminess due to climate change on coastal flooding; (3) coupling soil compaction
467 mechanics with time-series InSAR measurements to generate more reliable long-term ground deformation predictions; (4)
468 incorporating the ‘crowd sourced’ data and/or Unmanned Aerial Vehicle (UAV) remote sensing maps into flood model
469 calibration and validation, and (5) conducting quantitative assessment of coastal flood risk as well as cost-benefit analysis
470 of adaptation measures to support decision making with respect to financial investment. Finally, great efforts are required
471 to improve the accuracies in the datasets, models and future scenarios applied to coastal flood risk analysis.

472

473 **Acknowledgments**

474 This work was supported by the National Key Research and Development Program of China (Grant no: 2017YFE0100700),
475 the National Natural Science Foundation of China (Grant no: 41871164; 41801337; 51761135024), the Humanities and
476 Social Science Project of Education Ministry of China (Grant no: 17YJAZH111), the UK Natural Environment Research
477 Council under the Environmental Risks to Infrastructure Innovation Program (Grant no: NE/M008770/1; NE/N013050/1;
478 NE/R009600/1), the Key Laboratory of Land Subsidence Monitoring and Prevention, Ministry of Land and Resources
479 through Project KLLSMP201503, the Fund of the Director of the Key Laboratory of Geographic Information Science
480 (Ministry of Education), East China Normal University (Grant no: KLGIS2017C03), the Research Grants of Science and
481 Technology Commission of Shanghai Municipality through Project 18ZR1410800, and the National Science Foundation
482 of the United States (EAR-1520683). This work has been performed within the Dragon 4 ESA project ID 32294. Cosmo-
483 SkyMed SAR data were provided to us by the Italian Space Agency in the framework of the Dragon III project ID 10644
484 and TanDEM-X data were provided by the German Aerospace Center (DLR) under proposal NTI_INSA0405. Sentinel-1A
485 data were freely downloaded from the ESA Sentinel Hub.

486

487

488

489

490

491

492

493

494 **References**

495 Aly, M.H., Klein, A.G., Zebker, H., 2012. Land Subsidence in the Nile Delta of Egypt by persistent scatterer interferometry. Remote

496 Sensing Letters, 3(7), 621-630.

497 Antonioli, F., Anzidei, M., Amorosi, A., Presti, V. L., Mastronuzzi, G., Deiana, G., 2017. Sea-level rise and potential drowning of the
498 Italian coastal plains: Flooding risk scenarios for 2100. *Quaternary Science Reviews*, 158, 29-43.

499 Bamber, J.L., Riva, R.E., Vermeersen, B.L., Lebrocq, A.M., 2009. Reassessment of the potential sea-level rise from a collapse of the
500 west Antarctic ice sheet. *Science*, 324(5929), 901-903.

501 Bates, P.D., Roo, A.P.J.D., 2000. A simple raster-based model for flood inundation simulation. *Journal of Hydrology*, 236(1), 54-77.

502 Bates, P.D., Dawson, R.J., Hall, J.W., Horritt, M.S., Nicholls, R.J., Wicks, J., Hassan, M.A. A.M., 2005. Simplified two-dimensional
503 numerical modeling of coastal flooding and example applications. *Coast. Eng.* 52, 793-810.

504 Bates, P.D., Horritt, M., Fewtrell, T., 2010. A simple inertial formulation of the shallow water equations for efficient two-dimensional
505 flood inundation modeling. *Journal of Hydrology*, 387(1), 33-45.

506 Bamler, R.; Hartl, P, 1998. Synthetic aperture radar interferometry. *Inverse Problems*. 14, R1–R54.

507 Berardino, P., Fornaro, G., Lanari, R., Sansosti, E., 2002. A new algorithm for surface deformation monitoring based on small baseline
508 differential SAR interferograms. *Geoscience & Remote Sensing IEEE Transactions on*, 40(11), 2375-2383.

509 Bentley, C. R., 1998. Rapid sea-level rise from a west Antarctic ice-sheet collapse: a short-term perspective. *Journal of Glaciology*,
510 44(146), 157-163.

511 Bonano, M., Manunta M., Pepe, A., Paglia, L., Lanari, R., 2013. From previous C-Band to new X-Band SAR systems: Assessment of
512 the DInSAR Mapping improvement for deformation time-series retrieval in urban areas. *IEEE Transactions on Geoscience and*
513 *Remote Sensing*, 51(4), 1973-1984.

514 Cai, J.; Wang, J.; Wu, J.; Hu, C.; Grafaren, E.; Chen, J. Horizontal deformation rate analysis based on multiePOCH GPS measurements in
515 Shanghai. *J. Surv. Eng.* 2008, 134, 132–137.

516 Casu, F., Manzo, M., Lanari, R., 2006. A quantitative assessment of the SBAS algorithm performance for surface deformation retrieval
517 from DInSAR data. *Remote Sensing of Environment*, 102 (3), 195–210.

518 Carminati, E., Martinelli, G., 2002. Subsidence rates in the Po Plain, northern Italy: the relative impact of natural and anthropogenic
519 causation. *Engineering Geology*, 66(3), 241-255.

520 Casas, A., Lane, S.N., Yu, D., Benito, G., 2010. A method for parameterising roughness and topographic sub-grid effects in hydraulic
521 modeling from LiDAR data. *Hydrology & Earth System Sciences*, 14(8), 1567-1579.

522 Cayan, D.R., Bromirski, P.D., Hayhoe, K., Tyree, M., Dettinger, M. D., Flick, R.E., 2008. Climate change projections of sea level
523 extremes along the California coast. *Climatic Change*, 87(1), 57-73.

524 Chaussard, E., Wdowinski, S., Cabral-Cano, E., Amelung, F. Land subsidence in central Mexico detected by ALOS InSAR time-series
525 *Remote Sensing of Environment*, 140, 94-106.

526 Chen, C.W., Zebker, H.A., 2001. Two-dimensional phase unwrapping with use of statistical models for cost functions in nonlinear
527 optimization. *Journal of the Optical Society of America A Optics Image Science & Vision*, 18(2), 338-351.

528 Chen, W., 1991. Sediment transport and sediment dynamic environment of the mudflat with reference to the northern bank of the
529 Hangzhou Bay and Southern bank of Changjiang Estuary. *Acta Oceanologica Sinica*, 13, 813-821 (in Chinese).

530 Chen, Y., Shi Y., Li B., Yu J., 2016. Seawall subsidence in Shanghai: characteristics and driving mechanisms. *Marine Geology and*
531 *Quaternary Geology* 6, 71-78 (in Chinese).

532 Chu, T., Lindenschmidt K.E., 2017. Comparison and Validation of Digital Elevation Models Derived from InSAR for a Flat Inland Delta
533 in the High Latitudes of Northern Canada. *Canadian Journal of Remote Sensing*, 43(2), 109-123.

534 Cooper, M. J., Beevers, M. D., Oppenheimer M., 2008. The potential impacts of sea level rise on the coastal region of New Jersey, USA.
535 *Climatic Change*, 90, 475-492.

536 Costantini, M., Rosen, P. A., 1999. A generalized phase unwrapping approach for sparse data, in *Geoscience and Remote Sensing*
537 *Symposium, 1999. IGARSS '99 Proceedings. IEEE 1999 International, Hamburg*, 267-269.

538 Crosetto, M., Monserrat, O., Cuevas-González, M., Devanthy, N., Crippa, B., 2016. Persistent Scatterer Interferometry: A review.
539 *ISPRS Journal of Photogrammetry and Remote Sensing*, 115, 78-89.

540 Crosetto, M., Monserrat, O., Luzi, G., Cuevas, M., Devanthery, N., 2015. Deformation Monitoring Using Ground-Based SAR
541 Data. *Engineering Geology for Society and Territory - Volume 5*. Springer International Publishing.

542 Danielson, J.J., Gesch, D.B., 2010 (GMTED2010). Global Multi-Resolution Terrain Elevation Data. U.S. Geological Survey Open-File
543 Report; U.S. Geological Survey: Sioux Falls, SD, USA, 2011.

544 Du, X., Guo, H., Fan, X., Zhu, J., Yan, Z., Zhan, Q., 2016. Vertical accuracy assessment of freely available digital elevation models over
545 low-lying coastal plains. *International Journal of Digital Earth*, 9(3), 252-271.

546 Domeneghetti, A., 2016. On the use of SRTM and altimetry data for flood modeling in data - sparse regions. *Water Resources Research*,
547 52(4), 2901-2918.

548 Du, J., Yang, S., Feng, H., 2016. Recent human impacts on the morphological evolution of the Yangtze River delta foreland: A review
549 and new perspectives. *Estuarine Coastal & Shelf Science*, 181, 160-169.

550 Ericson, J.P., Vörösmarty, C.J., Dingman, S.L., Ward, L.G., Meybeck, M., 2006. Effective sea - level rise and deltas: Causes of change
551 and human dimension implications, *Global and Planetary Change*, 50, 63-82.

552 Fan, D., Wu, Y., Zhang, Y., Burr, G., Huo, M., Li, J., 2017. South flank of the Yangtze Delta: Past, present, and future. *Marine Geology*,
553 392, 78-93.

554 Fattahi, H., Amelung, F., Chaussard, E., Wdowinski, S., 2015. Coseismic and postseismic deformation due to the 2007 M5.5 Ghazaband
555 fault earthquake, Balochistan, Pakistan. *Geophysical Research Letters*, 42, 3305-3312.

556 Ferretti, C., Prati, C., Rocca, F., 2001. Permanent scatterers in SAR interferometry. *IEEE Transactions on Geoscience and Remote
557 Sensing*, 39(1), 8-20.

558 Ferretti, A. et al., "A new algorithm for processing interferometric datastacks: SqueeSAR," *IEEE Trans. Geosci. Remote Sens.*, vol. 49,
559 no. 9, pp. 3460–3470, Sep. 2011.

560 Franceschetti G, Lanari R, 1999. *Synthetic Aperture Radar Processing*, CRC Press.

561 Gesch, D.B., 1999. Chapter 31 – The effects of DEM generalization methods on derived hydrologic features, in Lowell, Kim, and Jatton,
562 Annick, eds., *Spatial Accuracy Assessment—Land Information Uncertainty in Natural Resources: Chelsea, Mich., Ann Arbor Press*,
563 255-262.

564 Goldstein, R.M., Werner, C.L., 1998. Radar interferogram filtering for geophysical applications. *Geophysical Research Letters*, 25(21),
565 4035-4038.

566 Gourmelen, N., Amelung, F., Casu, F., Manzo, M., Lanari, R., 2007. Mining-related ground deformation in Crescent Valley, Nevada:
567 implications for sparse GPS networks. *Geophysical Research Letters*, 34(9), 252-254.

568 Grilli, A., Spaulding, M.L., Oakley, B.A., Damon, C., 2017. Mapping the coastal risk for the next century, including sea level rise and
569 changes in the coastline: application to Charlestown RI, USA. *Natural Hazards*, (4), 1-26.

570 Gruber, A., Wessel, B., Huber, M., & Roth, A., 2012. Operational TanDEM-X DEM calibration and first validation results. *ISPRS Journal
571 of Photogrammetry & Remote Sensing*, 73(6), 39-49.

572 Hallegatte, S., Ranger, N., Mestre, O., Dumas, P., Corfee-Morlot, J., Herweijer, C., Wood R., 2011. Assessing climate change impacts,
573 sea level rise and storm surge risk in port cities: a case study on Copenhagen. *Climatic Change*, 104(1), 113-137.

574 Hay, C.C., Morrow, E., Kopp, R.E., Mitrovica, J.X., 2015. Probabilistic reanalysis of twentieth-century sea-level rise. *Nature*, 517, 481-
575 484.

576 Hinkel, J., Lincke, D., Vafeidis, A.T., Perrette, M., Nicholls, R. J., Tol, R. S. J., 2014. Coastal flood damage and adaptation costs under
577 21st century sea-level rise. *Proceedings of the National Academy of Sciences of the United States of America*, 111(9), 3292-3297.

578 Higgins, S.A., 2016. Review: Advances in delta-subsidence research using satellite methods. *Hydrogeology Journal*, 24(3), 587-600.

579 Hooper, A., Bekaert, D., Spaans, K., Arikan, M., 2012. Recent advances in SAR interferometry time series analysis for measuring crustal
580 deformation. *Tectonophysics*, 514, 1-13.

581 Horritt, M.S., Bates, P.D., 2001. Effects of spatial resolution on a raster based model of flood flow. *Journal of Hydrology*, 253(1–4), 239-
582 249.

583 Horton, R., Little, C., Gornitz, V., Bader, D., Oppenheimer, M., 2015. *New York City Panel on Climate Change 2015 Report Chapter 2:*

584 Sea Level Rise and Coastal Storms. *Annals of the New York Academy of Sciences*, 1336, 36-44.

585 IPCC, 2012. In: Field CB, Barros, V., Stocker, T.F., Qin, D., Dokken, D.J., Ebi, K.L., Mastrandrea, M.D., Mach, K.J., Plattner, G.K.,
586 Allen, S.K., Tignor, M., Midgley, P.M., (eds) *Manging the Risks of Extreme Events and Disasters to Advance Climate Change*
587 *Adaptation. A Special Report of Working Groups I and II of the Intergovernmental Panel on Climate Change*. Cambridge University
588 Press, Cambridge, p 582

589 IPCC, 2013. *Climate Change 2013: The physical science basis*. Cambridge: Cambridge University Press

590 IPCC, 2014. *Climate Change 2014: Synthesis Report. Contribution of Working Groups I, II and III to the Fifth Assessment Report of*
591 *the Intergovernmental Panel on Climate Change [Core Writing Team, R.K. Pachauri and L.A. Meyer (eds)]*. IPCC, Geneva,
592 Switzerland, 151 pp.

593 Jarvis, A., Reuter, H.I., Nelson, A., Guevara, E., 2008. Hole-filled SRTM for the globe Version 4. Available from the CGIAR-CSI SRTM
594 90m Database <<http://srtm.csi.cgiar.org>>.

595 Jelgersma, S., 1996. Land subsidence in coastal lowlands, in *Sea Level Rise and Coastal Subsidence*, edited by J. D. Milliman and B. U.
596 Haq, pp. 47-62, Kluwer Acad., Dordrecht, Netherlands.

597 Kampes, B.M., 2016. *Radar Interferometry: Persistent Scatterer Technique*; Springer: New York, NY, USA.

598 Kampes, B. M., Hanssen, R. F., Perski, Z., 2008. *Radar Interferometry with Public Domain Tools*. FRINGE 2003 Workshop (Vol.550).
599 FRINGE 2003 Workshop.

600 Karegar, M. A., Dixon, T. H., Malservisi, R., Kusche, J., Engelhart, S. E., 2017. Nuisance flooding and relative sea-level rise: the
601 importance of present-day land motion. *Scientific Reports*, 7(1), 11197.

602 Kopp, R.E., Horton, R.M., Little, C.M., 2014. Probabilistic 21st and 22nd century sea-level projections at a global network of tide-gauge
603 sites. *Earths Future*, 2 (8), 383-406.

604 Krieger, G., Moreira, A., Fiedler, H., Hajnsek, I., Werner, M., Younis, M., 2007. TanDEM-X: A satellite formation for high-resolution
605 SAR interferometry. *IEEE Transactions on Geoscience and Remote Sensing*, 45, 3317-3341.

606 Kubanek, J., Westerhaus, M., Schenk, A., Aisyah, N., Brotopuspito, K. S., & Heck, B., 2015. Volumetric change quantification of the
607 2010 merapi eruption using TanDEM-X InSAR. *Remote Sensing of Environment*, 164, 16-25.

608 Kubanek, J., Westerhaus, M., Heck, B. 2017. TanDEM-X time series analysis reveals lava flow volume and effusion rates of the 2012 –
609 2013 Tolbachik, Kamchatka fissure eruption. *Journal of Geophysical Research: Solid Earth*, 122, 7754-7774.

610 Lanari, R., Casu, F., Manzo, M., Zeni, G., Berardino, P., & Manunta, M., 2007. An overview of the small baseline subset algorithm: A
611 DInSAR technique for surface deformation analysis. *Pure & Applied Geophysics*, 164(4), 637-661.

612 Li, Y., Qin, Z., Duan, Y., 1998. An estimation and assessment of future sea level rise in Shanghai region. *Acta Geographica Sinica*, 53,
613 393-403 (in Chinese).

614 Lin, N., Emanuel, K., Oppenheimer, M., Vanmarcke, E., 2012. Physically based assessment of hurricane surge threat under climate
615 change. *Nature Climate Change*, 2(6), 462-467.

616 Lin, N., Emanuel, K., 2015. Grey swan tropical cyclones. *Nature Climate Change*, 6, 106-111.

617 Lin, N., Shullman, E., 2017. Dealing with hurricane surge flooding in a changing environment: part I. Risk assessment considering storm
618 climatology change, sea level rise, and coastal development. *Stochastic Environmental Research and Risk Assessment*, 31(9), 2379-
619 2400.

620 Little, C.M., Horton, R. M., Kopp, R. E., Oppenheimer, M., Vecchi, G. A., Villarini, G. 2016. Joint projections of US East Coast sea
621 level and storm surge. *Nature Climate Change*, 5(12), 1114-1120.

622 Liu, X., 2008. *Shanghai flood prevention handbook*. Shanghai: Shanghai Popular Science Press (in Chinese).

623 Mason, D.C., Trigg, M., Garcia-Pintado, J., Cloke H. L., Neal J., Bates P. D., 2016. Improving the TanDEM-X Digital Elevation Model
624 for flood modeling using flood extents from Synthetic Aperture Radar images. *Remote Sensing of Environment*, 173, 15-28.

625 Massonnet, D. and Feigl, K. L., 1998. Rader interferometry and its application to changes in the Earth's surface, *Reviews of Geophysics*,
626 36, 441-500.

627 Meyer, D.J., Tachikawa, T., Abrams, M., Tsu, H., Hato, M., Gesch, D.B., 2011. The ASTER Global Digital Elevation Model version 2.0

628 - Early Validation Results. AGU Fall Meeting (Vol.20, pp.1442). AGU Fall Meeting Abstracts.

629 Mills, M., Mutafoğlu, K., Adams, V.M., Archibald, C., Bell, J., Leon, J.X., 2016. Perceived and projected flood risk and adaptation in
630 coastal southeast Queensland, Australia. *Climatic Change*, 136(3-4), 523-537.

631 Mora, O., Mallorqui, J.J., Broquetas, A., 2003. Linear and nonlinear terrain deformation maps from a reduced set of interferometric SAR
632 images. *IEEE Transactions on Geoscience & Remote Sensing*, 41(10), 2243-2253.

633 Mukherjee, S., Joshi, P., Mukherjee, S., Ghosh, A., Garg, R., Mukhopadhyay, A., 2013. Evaluation of vertical accuracy of open source
634 Digital Elevation Model (DEM). *Int. J. Appl. Earth Obs. Geoinf.* 21, 205-217.

635 Orton, P., Vinogradov, S., Georgas, N., Blumberg, A., Lin, N., Gornitz, V., Little, C., Jacob, K., Horton, R., 2015. New York City Panel
636 on Climate Change 2015 Report Chapter 4: Dynamic coastal flood modeling. *Annals of the New York Academy of Sciences*,
637 1336(1), 56-66.

638 Oppenheimer, M., Alley, R. B., 2016. How high will the seas rise? *Science*, 354, 1375-1377.

639 Paprotny, D., Terefenko, P., 2017. New estimates of potential impacts of sea level rise and coastal floods in Poland. *Nat. Hazards*. 85,
640 1259-1277.

641 Pepe, A. and Lanari R., 2006. On the Extension of the Minimum Cost Flow Algorithm for Phase Unwrapping of Multitemporal
642 Differential SAR Interferograms. *IEEE Transactions on Geoscience and remote sensing*, 44(9), 2374-2383.

643 Pepe, A., Solaro, G., Calò, F., Dema, C., 2016b. A Minimum Acceleration Approach for the Retrieval of Multiplatform InSAR
644 Deformation Time Series. *IEEE Journal of Selected Topics in Applied Earth Observations & Remote Sensing*, 9(8), 3883-3898.

645 Pepe, A., Bonano M., Zhao Q., 2016a. The use of C-/X-band time-gapped SAR data and geotechnical models for the study of Shanghai's
646 ocean-reclaimed lands through the SBAS-DInSAR technique. *Remote Sensing* 8(11), 911.

647 Pfeffer, W. T., Harper, J. T., O'Neel, S., 2008. Kinematic constraints on glacier contributions to 21st-century sea-level rise. *Science*,
648 321(5894), 1340-3.

649 Ridley, J., Gregory, J. M., Huybrechts, P., Lowe, J., 2010. Thresholds for irreversible decline of the Greenland ice sheet. *Climate*
650 *Dynamics*, 35(6), 1049-1057.

651 Ritz, C., Edwards, T. L., Durand, G., Payne, A. J., Peyaud, V., Hindmarsh, R. C. A., 2015. Potential sea-level rise from Antarctic ice-
652 sheet instability constrained by observations. *Nature*, 528, 115-118.

653 Sampson, C.C., Smith, A.M., Bates, P.D., Neal, J.C., Lorenzo, A., Freer, J.E., 2015. A high-resolution global flood hazard model. *Water*
654 *Resources Research*, 51(9), 7358-7381.

655 Samsonov, S., d'Oreye, S., 2012. Multidimensional time-series analysis of ground deformation from multiple InSAR data sets applied
656 to Virunga Volcanic Province. *Geophys. J. Int.*, 191, 1095–1108.

657 State Oceanic Administration of People's Republic of China, 2008. China sea level bulletin 2007 (in Chinese).

658 State Oceanic Administration of People's Republic of China, 2017. China sea level bulletin 2016 (in Chinese).

659 Syvitski, J. P. M., Kettner, A. J., Overeem, I., Hutton, E. W. H., Hannon, M. T., Brakenridge, G. R., 2009. Sinking deltas due to human
660 activities. *Nature Geoscience*, 2(10), 681-686.

661 Tachikawa, T., Hato, M., Kaku, M., Iwasaki, A., 2011. Characteristics of ASTER GDEM version 2. In: *Geoscience and Remote Sensing*
662 *Symposium (IGARSS)*, 2011 IEEE International, IEEE, 3657-3660.

663 Tarekegn, T. H., Haile, A. T., Rientjes, T., Reggiani, P., Alkema, D., 2010. Assessment of an ASTER-generated DEM for 2D
664 hydrodynamic flood modeling. *International Journal of Applied Earth Observation & Geoinformation*, 12(6), 457-465.

665 Teatini, P., Tosi, L., Strozzi, T., 2011. Quantitative evidence that compaction of Holocene sediments drives the present land subsidence
666 of the Po Delta, Italy. *Journal of Geophysical Research Solid Earth*, 116(B8), 407-416.

667 Tian, B., Wu, W.T., Yang, Z.Q., Zhou, Y.X., 2016. Drivers, trends, and potential impacts of long-term coastal reclamation in China from
668 1985 to 2010. *Estuarine Coastal and Shelf Science*, 170, 83-90.

669 Usai, S., 2003. A least squares database approach for SAR interferometric data. *IEEE Transactions on Geoscience & Remote Sensing*,
670 41(4), 753-760.

671 Vaughan, D.G., Spouge, J.R., 2002. Risk estimation of collapse of the west Antarctic ice sheet. *Climatic Change*, 52(1-2), 65-91.

672 Wang, J., Gao, W., Xu, S., Yu, L., 2012. Evaluation of the combined risk of sea level rise, land subsidence, and storm surges on the
673 coastal areas of Shanghai, China. *Climatic Change*, 115, 537–558.

674 Weigt, M., Rizzoli, P., Bachmann, M., Bräutigam, B., Schulze, D., 2012. TanDEM-X mission — interferometric performance and global
675 DEM acquisition status. Radar 2012, IET International Conference on Radar Systems, Glasgow, UK, 22-25, Oct. 2012.

676 Wessel, P., Smith, W.H.F., Scharro, R., Luis, J.F., Wobbe, F., 2013. Generic Mapping Tools: Improved version released. *EOS Transactions*,
677 *American Geophysical Union* 94, 409–410.

678 Shi, Y., Zhu, J., Xie, Z., Ji, Z., Jiang, Z., Yang, G., 2012. Prediction and prevention of the impacts of sea level rise on the Yangtze River
679 Delta and its adjacent areas. *Science in China, Series D: Earth Sciences*, 43, 412-422.

680 Yang, L., Meng, X., Zhang, X., 2011. SRTM DEM and its application advances. *International Journal of Remote Sensing*, 32 (14), 3875-
681 3896.

682 Yang, S., Milliman, J.D., Li, P., Xu, K., 2011. 50,000 dams later: Erosion of the Yangtze River and its delta. *Global Planetary Change*,
683 75, 14-20.

684 Yang, Y.-Q. Tang, N.-Q. Zhou, and J.-X. Wang, “Consolidation settlement of Shanghai dredger fill under self-weight using centrifuge
685 modeling test,” *J. Cent. South Univ. Technol.*, vol. 39, no. 4, pp. 862–866, Aug. 2008 (in Chinese).

686 Yin, J., Yu, D., Yin Z., 2016a. Evaluating the impact and risk of pluvial flash flood on intra-urban road network: a case study in the city
687 center of Shanghai, China. *Journal of Hydrology*, 537, 138-145.

688 Yin, J., Lin, N., Yu, D., 2016b. Coupled modeling of storm surge and coastal inundation: a case study in New York City during Hurricane
689 Sandy. *Water Resources Research*, 52, 8685-8699.

690 Yin, J., Yu, D., Yin Z., Wang, J., Xu, S., 2013. Modeling the combined impacts of sea-level rise and land subsidence on storm tides
691 induced flooding of the Huangpu River in Shanghai, China. *Climatic Change*, 119(3), 919-932.

692 Yoon, Y.T., Eineder, M., Yague-Martinez, N., Montenbruck, O., 2009. TerraSAR-X precise trajectory estimation and quality assessment.
693 *IEEE Transactions on Geoscience and Remote Sensing*, 47, 1859-1868.

694 Yu, D., Lane, S.N., 2006a. Urban fluvial flood modeling using a two-dimensional diffusion wave treatment, part 1: mesh resolution
695 effects. *Hydrological Processes*, 20, 1541-1565.

696 Yu, D., Lane, S.N., 2006b. Urban fluvial flood modeling using a two-dimensional diffusion wave treatment, part 2: development of a
697 sub grid-scale treatment. *Hydrological Processes*, 20, 1567-1583.

698 Yu, D., Lane, S.N., 2011. Interaction between subgrid-scale resolution, feature representation and grid-scale resolution in flood
699 inundation modeling. *Hydrological Processes*, 25, 36-53.

700 Yu, L., Yang T., Zhao Q., Liu M. and Pepe, A. 2017. The 2015-2016 Ground Displacements of the Shanghai Coastal Area Inferred from
701 a Combined COSMO-SkyMed/Sentinel-1 DInSAR Analysis. *Remote Sens.*, 9, 1194.

702 Zhao, Q., Pepe, A., Gao, W., Lu, Z., Bonano, M., He, M., Wang, J., Tang, X., 2015. A DInSAR Investigation of the Ground Settlement
703 Time Evolution of Ocean-Reclaimed Lands in Shanghai. *IEEE Journal of Selected Topics in Applied Earth Observations & Remote*
704 *Sensing*, 8(4), 1763-1781.

705 Zuo, S., Bei, L., Yang, H., 2007. Topography evolution and analysis of Nanhui nearshore. *Journal of Waterway & Harbor*. 28 (2), 108-
706 112.